Electronic Supporting Information (ESI)

High-temperature reconstruction of carbon nanotubes with iron impurity as built-in catalysts for potent electrical conductive additives in supercapacitor electrodes

Keyang Li[a, b, ‡], Yunfeng Feng[a, c, ‡], Qi Zhang[a], Yiqing Guo[d], Jianing Gan[a], Yilun Huang[e, *], Menghao Yang[f, *], Ming Zhao[a], Daming Zhuang[a], Qianming Gong[a, *]

[a] Key Laboratory for Advanced Materials Processing Technology, School of Materials Science and Engineering, Tsinghua University, Beijing 100084, P.R. China.

[b] School of Materials Science and Engineering, Peking University, Beijing 100871, P.R. China

[c] School of Materials Sciences and Technology, China University of Geosciences, Beijing 100083, China.

[d] School of Chemistry and Chemical Engineering, Beijing Institute of Technology, Beijing 100084, P. R. China.

[e] SINOPEC Beijing Research Institute of Chemical Industry, Beijing 100013, P.R. China.

[f] School of Materials Science and Engineering, Tongji University, Shanghai 201804, P. R. China.

[‡] These authors contributed equally to this work.

Experimental section:

1. High-temperature reconstruction process of the CNTs-3000 (**Fig. S1**):

The commercial carbon nanotubes were subjected to high-temperature thermal treatment in a high-temperature graphitization furnace. The detailed procedure is as follows: approximately 500 mg of the pristine CNT powder was placed in a high-purity graphite crucible, which was then loaded into the furnace chamber.

Atmosphere and pressure control: From room temperature to 1400 °C, the furnace was maintained under a high vacuum (pressure < 10^{-2} Pa) with a heating rate of 10 °C·min^{-1}. Over the temperature range of 1400 °C to 3000 °C, a flowing high-purity argon (Ar, 99.999%) atmosphere was introduced and maintained at a slight positive pressure (approximately 1.05 atm) to prevent air ingress. The heating rate in this stage was 5 °C·min^{-1}.

Dwell time and cooling: The sample was held at the target temperature of 3000 °C for 1 hour to ensure complete reconstruction and graphitization. After the heat treatment, the sample was furnace-cooled naturally to room temperature.

Sample mass and yield: The typical mass of the starting pristine CNTs per batch was ~500 mg. The mass of the final CNTs-3000 product was ~475 mg, corresponding to a high mass yield of >95%.

Safety measures: Standard safety protocols for high-temperature operations were strictly followed. The furnace system is equipped with automatic over-temperature shutdown and over-pressure release safety devices. The entire process was conducted under an inert atmosphere to prevent combustion.

The pristine commercial carbon nanotubes are designated as CNTs. The modified carbon nanotubes after the 3000 °C high-temperature treatment are designated as CNTs-3000.

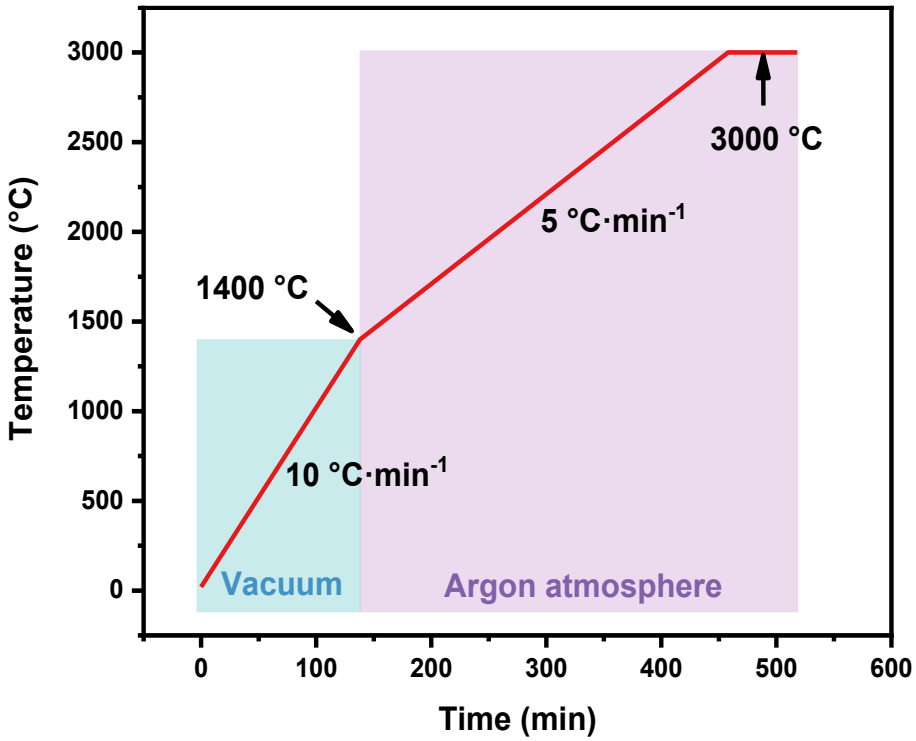

Fig. S1 Processing program of the high-temperature reconstruction of CNTs-3000.

Coin-type supercapacitor preparing process.

1. Pre-experiment preparation

Materials and reagents:

Electrode material: working electrode discs (Ni form coated with active material).

Counter/reference electrode: identical electrode discs.

Separator: glass fiber separator or celgard polypropylene separator (diameter ~19 mm).

Electrolyte: 1 M $TEABF_4$ in acetonitrile (AN).

Coin cell parts: CR2032 components.

High-purity argon gas (>99.99%).

2. Assembly procedure

Electrode preparation and drying:

The electrode slurry was prepared with a mass ratio of 80:10:10 for active material (AC), conductive agent, and binder (polyvinylidene fluoride, PVDF), respectively. First, the PVDF binder was dissolved in a suitable amount of N-Methyl-2-pyrrolidone solvent under magnetic stirring until a clear solution was obtained. The conductive agent was then added, and the mixture was stirred using a centrifugal mixer at 2000 rpm for 30 minutes to form a homogeneous conductive paste. Finally, the active material was added in batches and mixed at 2000 rpm for at least 2 hours until a uniform, particle-free slurry was achieved. The solid content of the slurry was adjusted to approximately 30-40%. The cleaned and dried current collector was fixed on a coater, and the slurry was uniformly coated onto the foil using the doctor blade method, with the wet film thickness controlled by fixed-thickness spacers;

The coated electrode was initially dried in an air-blowing oven at 60 °C for 30 minutes and then transferred to a vacuum oven for final drying at 80 °C under vacuum for 12 hours to thoroughly remove residual solvent and moisture. The dried electrode sheets were calendared using a rolling press at a pressure of 5 MPa to enhance electrode density and adhesion to the current collector;

Punch the electrode sheets into small discs with a diameter of 10 mm;

Precisely weigh and record the mass of each electrode disc;

Place the punched electrode discs and separators in a vacuum oven and dry under vacuum at 90 °C for 12 hours to thoroughly remove moisture;

Transfer all dried components (electrode discs, separators, cell case parts, excluding electrolyte) into the antechamber of the glove box;

After the purge-fill cycles, move the components into the main working area of the glove box;

Place the electrolyte inside the glove box to equilibrate for at least 30 minutes.

3. Cell Assembly:

Take a negative can serving as the positive electrode in this two-electrode test configuration;

Place one punched electrode disc (active material facing up) into the center of the negative can;

Inside the glove box, immerse the dried separators in the pure solvent of the electrolyte used (1 M $TEABF_4$/AN) for approximately 30 s. Then, remove and gently blot the surface with a lint-free wipe to remove excess solvent before assembly;

Using tweezers, carefully place a separator on top of the electrode disc;

Using a pipette, drop 100 μL of electrolyte onto the separator. Ensure the separator is fully wetted, but avoid overflow;

Align and place the other electrode disc (active material facing down) onto the wetted separator, forming a “sandwich” structure;

Place the spacer and then the spring sheet sequentially;

Cover the assembly with the positive can (the can with the gasket groove), ensuring all components are properly aligned.

4. Crimping/sealing:

Carefully transfer the assembled cell components into the die of the coin cell crimping machine;

Apply appropriate pressure (1.0 MPa) and maintain for 10-30 seconds to ensure the cell is completely sealed;

Remove the crimped cell and inspect the sealing edge for uniformity, ensuring no deformation or signs of leakage;

5. Ageing and pre-test preparation:

Remove the sealed cells from the glove box;

Before electrochemical testing, let the cells stand (age) at room temperature for at least 6 hours to allow the electrolyte to fully infiltrate and distribute within the electrodes.

2. Characterization

The morphology and structure of samples were analyzed by scanning electron microscope (SEM, Merlin Compact from Zeiss) and transmission electron microscope (TEM, JEM-2100 F). Thermogravimetric (TG) analysis was performed by a thermogravimetric analyzer (TA instruments, Q5000IR). Raman spectrometry (Horiba HR800), X-ray diffraction (XRD, Rigaku D/max-2500/PC) were executed to determine the graphitization degree and lattice information. Elemental analysis was accomplished by X-ray photoelectron spectroscopy (XPS, Thermo Scientific Escalab 250XI) and X-ray Fluorescence Spectroscopy (XRF, Shimadzu XRF-1800). Low-field nuclear magnetic resornance tests (LD-NMR, VTMR20-010V-I) were executed to determine the dispersion stability of the samples. The conductivity measurements were fulfilled by the Hall effect measurement system (Accent HL5500).

The interplanar distances of graphite (002) were calculated by the Bragg's equation[1]:

$$d_{(002)} = \frac{\lambda}{2sin\theta} \qquad (s1)$$

3. Electrochemical preparation measurements

Most electrochemical measurements were performed on the BioLogic SAS VSP-300 electrochemical station and the electric capacity was performed on the Arbin BT 2000 capacity measurement platform. Capacitance performances of the electrodes were investigated in 1.0 mol·L^{-1} $TEABF_4$/AN electrolyte. To fabricate the electrodes, AC and conductive additives were mixed in N-methyl-2-pyrrolidone (NMP, the mass ratio of AC and conductive additives was 8:1). After ultrasonic dispersion for 20 minutes, the mixture was filtered out and freeze-dried. Then the mixture and 10 % PVDF were ground to get a uniform electrode paste. Then paste was evenly coated on a 1 cm^2 nickel foam, dried at 120 °C and tableted under a pressure of 50 kg·cm^{-2} to fabricate electrodes. The mass specific capacitance of the three-electrode system was calculated using the following formula[2]:

$$C_{ms} = \frac{I_m \Delta t}{\Delta V} \qquad (s2)$$

where C_{ms} is the mass specific capacitance (F g^{-1}), I_m (A g^{-1}) and Δt (s) are the discharge current density and discharge time, respectively, and ΔV (V) refers to the potential

change in discharge.

The energy density and power density were calculated based on the following equations[3]:

$$E = \frac{C_{ms}\Delta V^2}{(2 \times 3.6)} \quad (s3)$$

$$P = \frac{E \times 3600}{\Delta t} \quad (s4)$$

where E (W h kg^{-1}) is the energy density and P (W kg^{-1}) is the power density of the system.

The ion diffusion coefficient and practical power density of devices could be calculated according to the equation:

$$i(V) = k_1\nu + k_2\nu^{\frac{1}{2}} \quad (s5)$$

$$P_{max} = \frac{V^2}{4 \cdot ESR \cdot m} \quad (s6)$$

Where i is current density (A g^{-1}), ν (mV·s-1) and V (V) are the sweeping rate and potential. Also, $k_1\nu$ and $k_2\nu^{1/2}$ represent surface-controlled and diffusion-controlled processes respectively.

4. MD Simulation methods

The molecular dynamics simulations are carried out by modified LAMMPS code. The initial configuration of CNT-Fe system is shown in **Fig. S4.** The diameter of the SW-CNT is 2.4 nm and the length is 16 nm. The defects in the CNT contains vacancies and five-seven rings. The γ-Fe particle with diameter of 1.2 nm is put adjacent to the lattice vacancies. The Tersoff/zbl potential developed by Henriksson[4] is adopted to describe the interaction between atoms. Periodical boundary conditions are used during the simulation within the NPT ensemble. The length of the box perpendicular to the axis of the CNT is set to be large enough to avoid the interaction between atoms from different boxes. The pressure and the temperature are controlled by Nose/Hoover barostat and thermostat. In order to restrain the rotation of the SW-CNT, the velocity perpendicular to the axis of the CNT for the atoms at the ends of the CNT is set to zero. The time step is set to be 1fs. The initial temperature is 300K. The Fe-CNT is heated up to 1500K, then 2500K and at last 3500K at a heating rate of 0.1K/fs. The temperature is kept at 1500K and 3500K for 3μs.

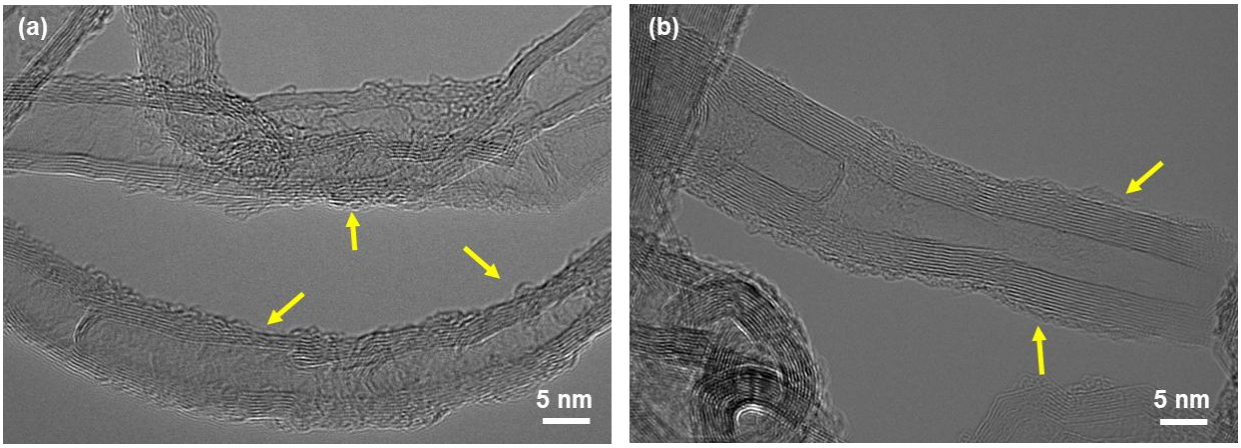

Fig. S2 HR-TEM images of CNTs (a) and CNTs-3000 (b).

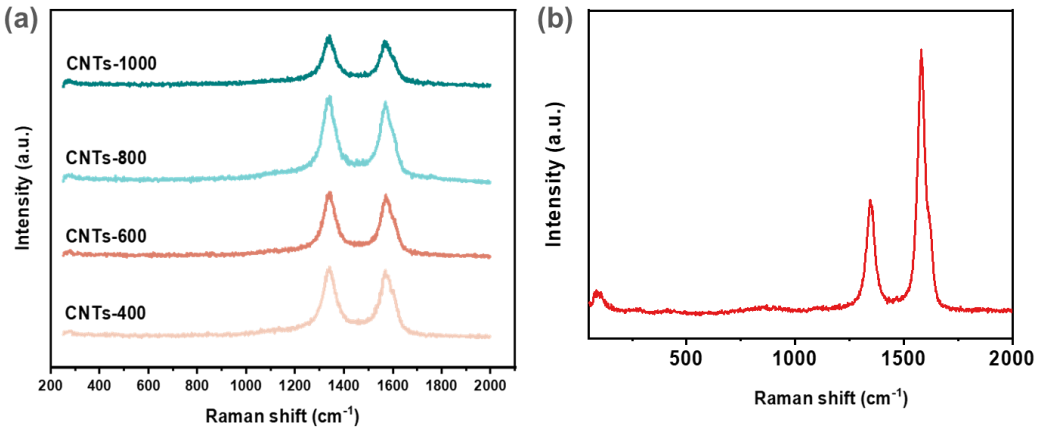

Fig. S3 Raman spectra of the CNTs samples treated at lower temperatures (a) and CNTs-Fe-free-3000 (b).

Note: we performed identical heat treatments on the same commercial CNTs at lower temperatures (400, 600, 800, and 1000 °C) and CNTs-Fe-free-3000 to evaluate the necessity of the 3000 °C treatment and iron impurity. The Raman spectra result of these samples (included as **Fig. S3**) reveal a key finding: the I_D/I_G ratio remains largely unchanged (around 1.05-1.10) at these conventional annealing temperatures. This demonstrates that modest thermal treatment alone is insufficient for significant defect repair in our system even though it contains iron impurity. And after the removal of iron impurity, the I_D/I_G value of 3000 ℃ treated Fe-free-CNTs (0.72) is still higher than that of CNTs-3000 (0.61), confirming that the treatment under both high-temperature and existence of iron impurities is effective in decreasing defect and enhancing graphitization degree of CNTs.

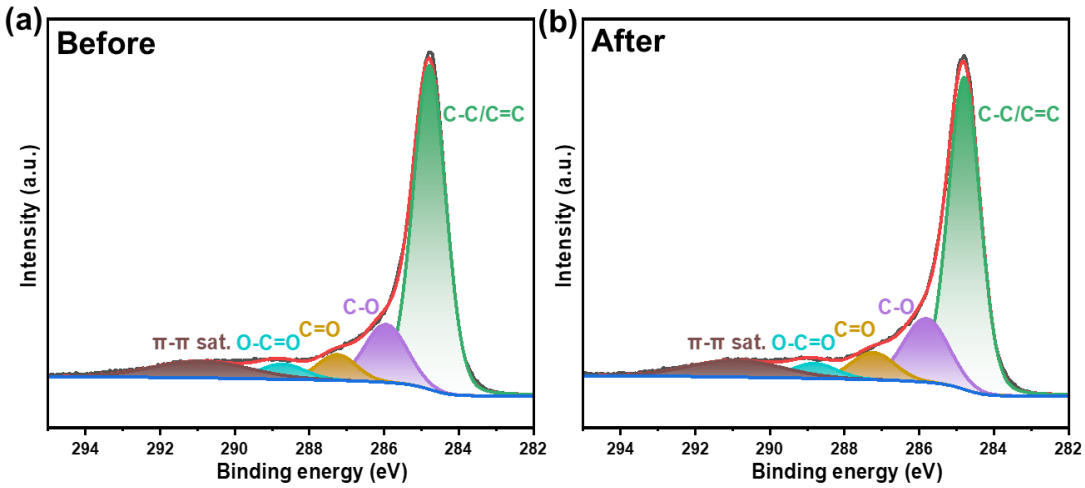

Fig. S4 Deconvoluted XPS C 1s peaks before (a) and after (b) the cycling.

Note: The C-O composition of the electrode active materials is slightly enhanced after the cycling (**Fig. S4**), which could be attributed to the "electrochemical activation" effects during the cycling tests under high current density and these effects would result in the boosted capacitance retention over 100% shown in **Fig. 3e.** Meanwhile, the other components stayed relatively stable, indicating the excellent durability and stability of the electrode active materials and conductive agents under the harsh tests.

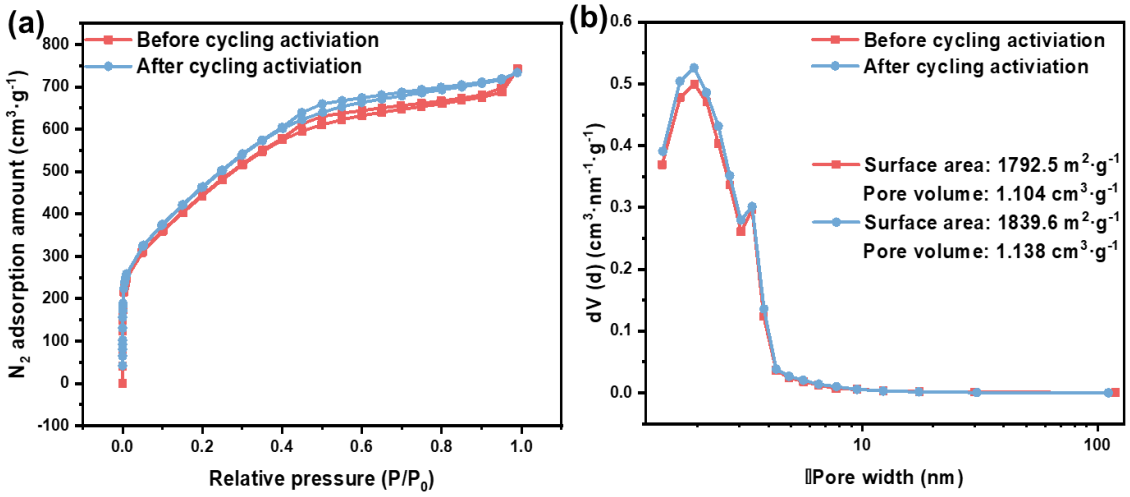

Fig. S5 N_2 adsorption isotherms (a) and pore width distribution (b) of the active materials before and after cycling.

Note: The specific surface area and pore volume of the electrode active materials slightly enhanced after the cycling (**Fig. S5**), which further evidenced "electrochemical activation" process happened and optimized the wettability and pore structures of the materials, which also resulted in the boosted capacitance retention over 100% shown in **Fig. 3e**.

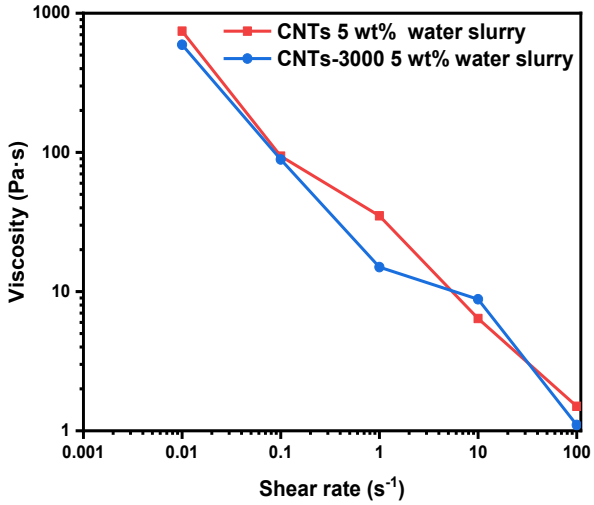

Fig. S6 resistance-rheology curves of CNTs and CNTs-3000 water slurries.

Note: According to the viscosity of different slurries under different shear rates (**Fig. S6**), we could find that CNTs and CNTs-3000 water slurries exhibited similar rheological behavior and their viscosities under different shear rates are close, so their processability should be similar and all the testing results are comparable.

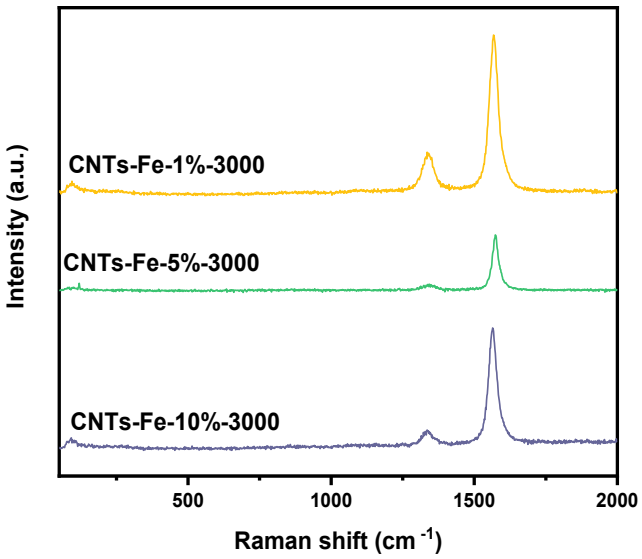

Fig. S7 Raman spectroscopy of the gradient-Fe-doped samples.

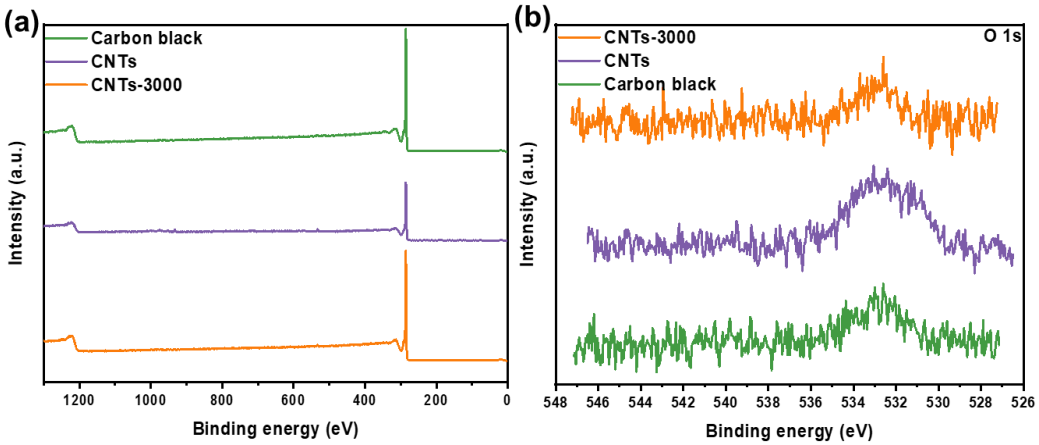

Fig. S8 XPS survey (a) and O 1s peaks (b) of the samples.

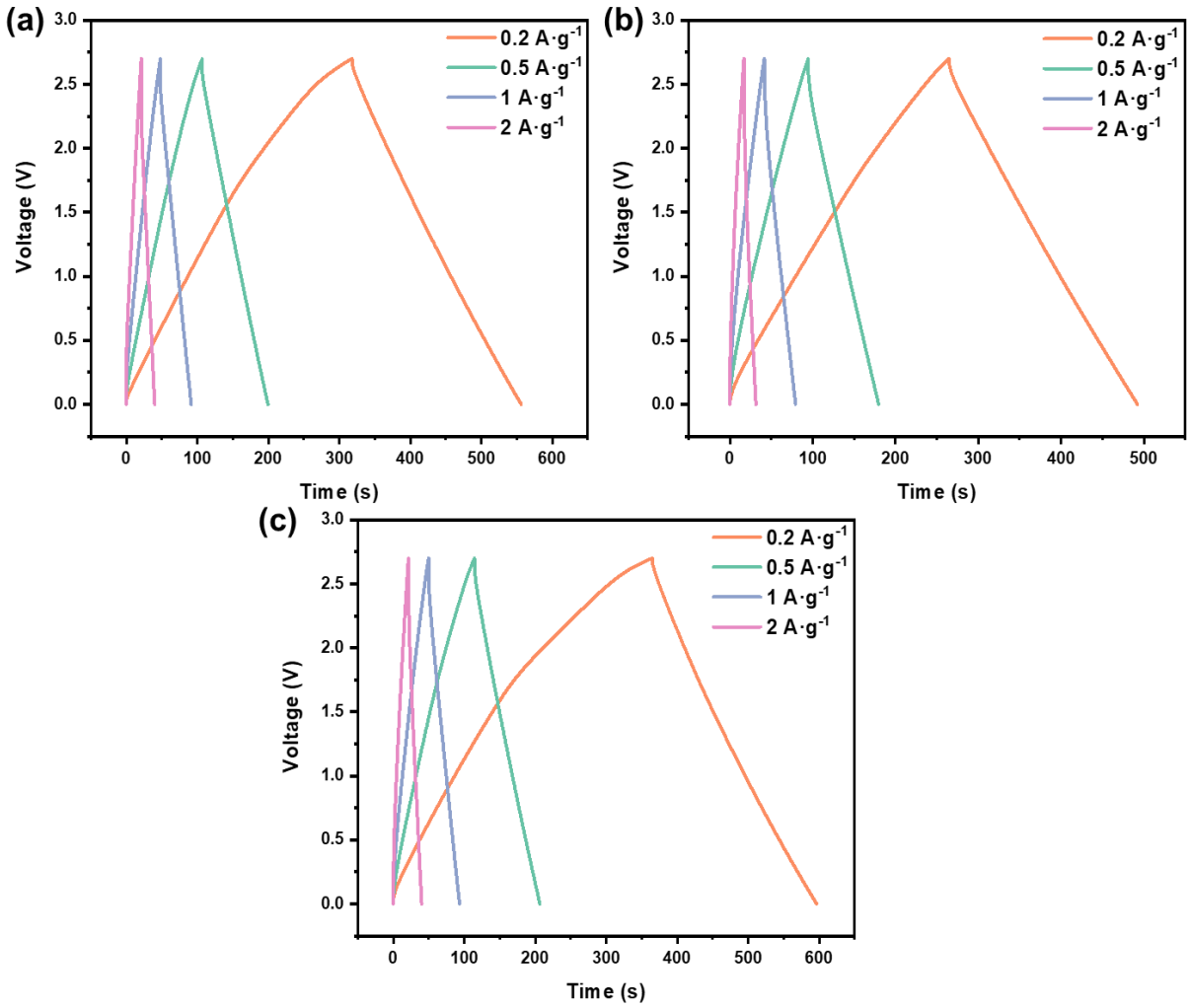

Fig. S9 GCD curves of (a) AC/CNTs, (b) AC/CNTs-3000, and (c) AC/Carbon black electrodes.

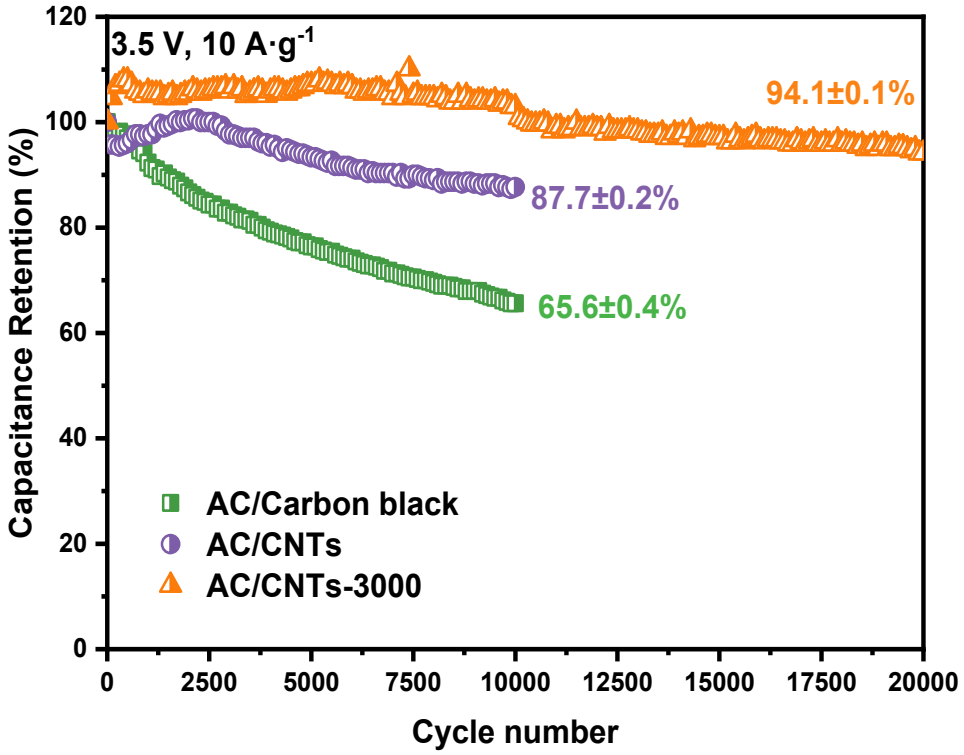

Fig. S10 Capacitance retention of the prepared electrodes under 3.5 V voltage at 10 $A \cdot g^{-1}$ current density.

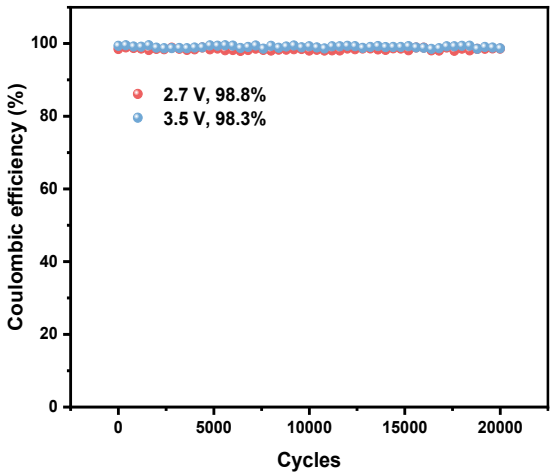

Fig. S11 Coulombic efficiencies under 3.5 V and 2.7 V for AC/CNTs-3000 supercapacitors after 20000 cycles.

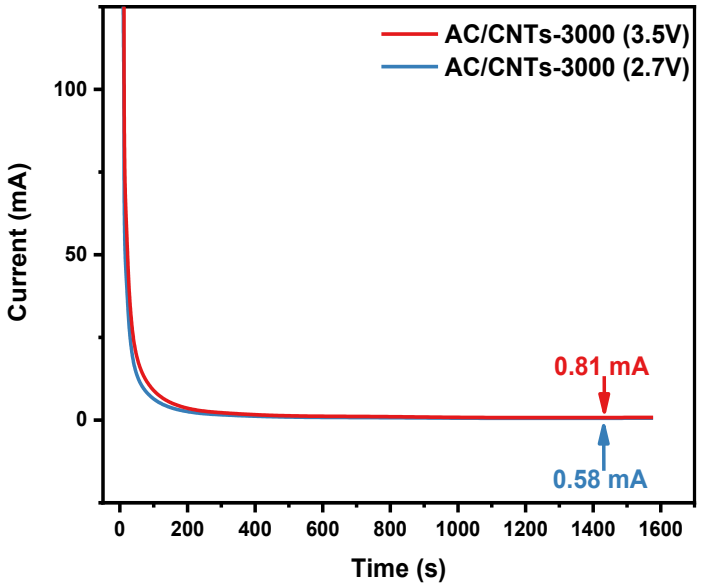

Fig. S12 Leakage current curves under 3.5 V and 2.7 V for AC/CNTs-3000 supercapacitors

Note: The leakage current curves in **Fig. S12** exhibit a very low leakage current under different voltages (0.81 mA@ 3.5 V and 0.58 mA@ 2.7 V), providing direct evidence that the excellent capacity retention during long-term cycling is underpinned by superior interfacial stability and minimal parasitic reactions.

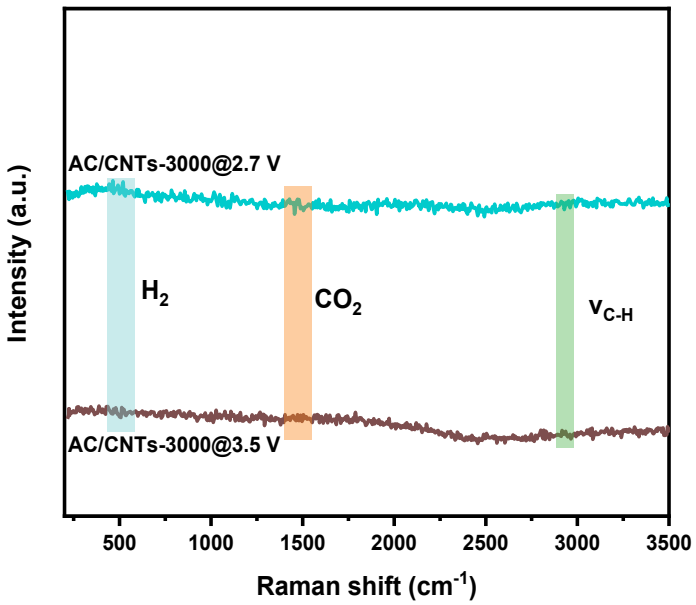

Fig. S13 Gas-phase Raman spectroscopy of AC/CNTs-3000 under 2.7 V and 3.5 V.

Note: Gas-phase Raman spectroscopy results shown **Fig. S13** reveal that even under relatively high voltage, there is still no significant Raman-active vibration peaks could be observed, which indicates the high stability of AC/CNTs-3000 electrodes.

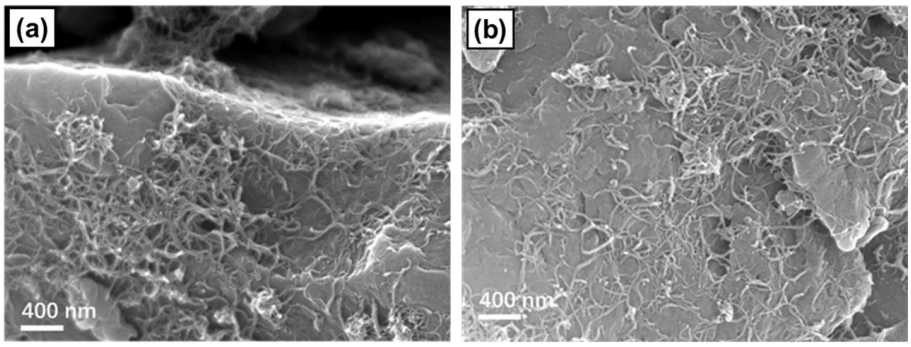

Fig. S14 SEM images of conductivity agents after 20000 cycles under 2.7 **(a)** and 3.5 V voltage **(b)**.

Note: No significant agglomeration, distortion or damage could be observed for the CNTs-3000 conductive agents after 20000 cycles under 2.7 V and 3.5 V voltage (**Fig. S14**), demonstrating its high stability.

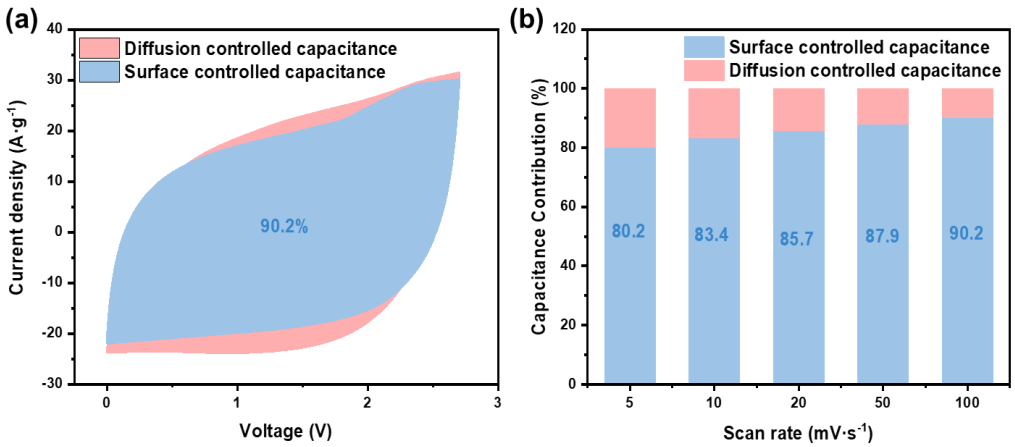

Fig. S15 (a) Separation of the surface-controlled contribution and diffusion-controlled contribution for the AC/CNTs-3000 electrode at 100 mV s^{-1}; **(b)** Contributions of diffusion-controlled and surface-controlled capacitances of AC/CNTs-3000 under different scan rates.

Note: According to the CV curves in Fig. S15a, we could find that there is no distinct redox peak and thus parasitic reactions might not happen or not detectable at least, so we further figured out the contribution of diffusion-controlled and surface-controlled capacitances as shown in **Fig. S15** according to the reviewer's suggestion**.** It demonstrates that the electrochemical performance of AC/CNTs-3000 electrode is mainly dominated by surface-controlled capacitance, which means that AC-CNTs-3000 exhibits a typical electronic-double-layer-capacitor (EDLC) type behavior, with nearly no pseudocapacitance contribution or parasite reactions.

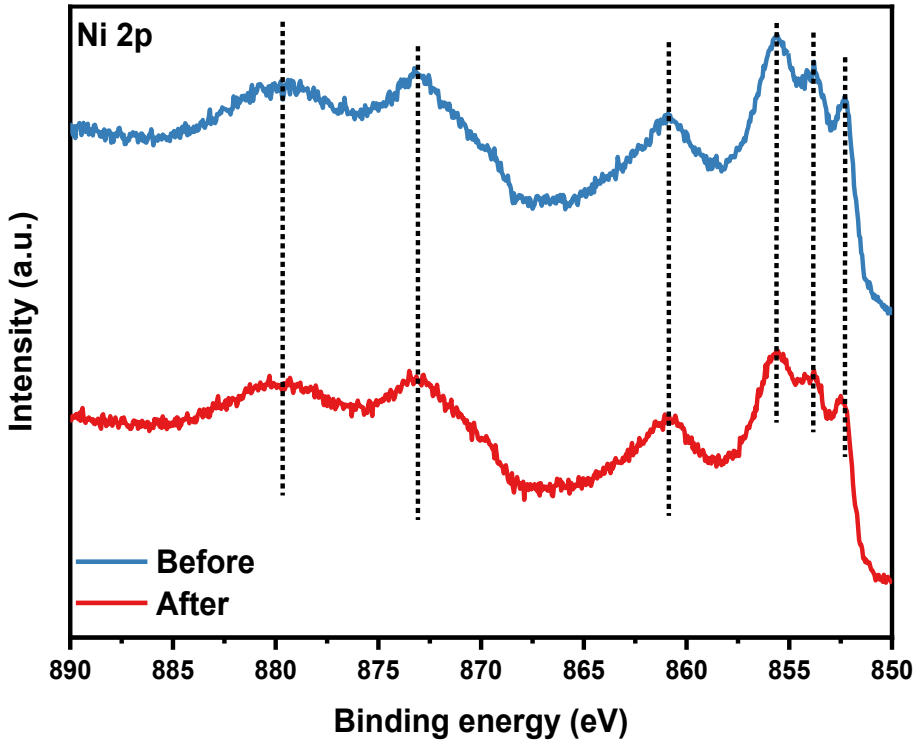

Fig. S16 XPS Ni 2p peaks of the Ni foam current collectors before **(a)** and after **(b)** cycling.

Note: XPS Ni 2p peaks of the Ni foam before and after cycling (**Fig. S16**) indicate the stability of Ni foam as current collectors for supercapacitor electrodes under galvanostatic charging/discharging cycling tests, as no obvious variation of the peaks could be observed.

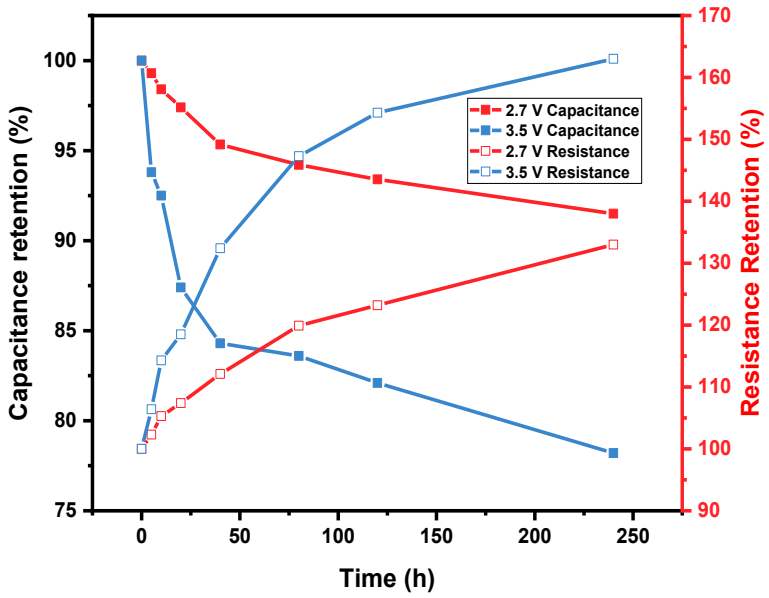

Fig. S17 Capacitance and resistance retention of the supercapacitors under 3.5 V and 2.7 V in the 240-h float charging tests.

Note: Capacitance and resistance retention of the supercapacitors under 3.5 V and 2.7 V in the 240-h float charging tests in **Fig. S17** exhibit that at relatively lower voltage (2.7 V), a better capacitance retention and lower resistance increase could be obtained, which could be attributed to the inhibited ageing of electrode under low voltage.

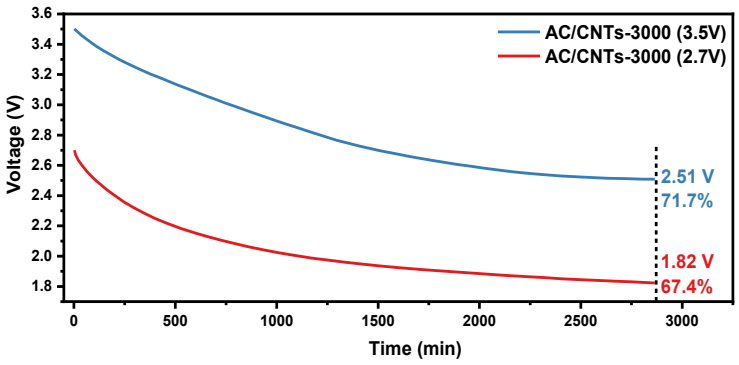

Fig. S18 Self-discharge curves under 3.5 V and 2.7 V for AC/CNTs-3000 supercapacitors

Note: The self-discharge curves in **Fig. S18** exhibit relatively high voltage retention after 2800 min self-discharge (71.7%@ 3.5 V and 67.4%@ 2.7 V), providing a high tendency of excellent stability in AC/CNTs-3000 supercapacitors.

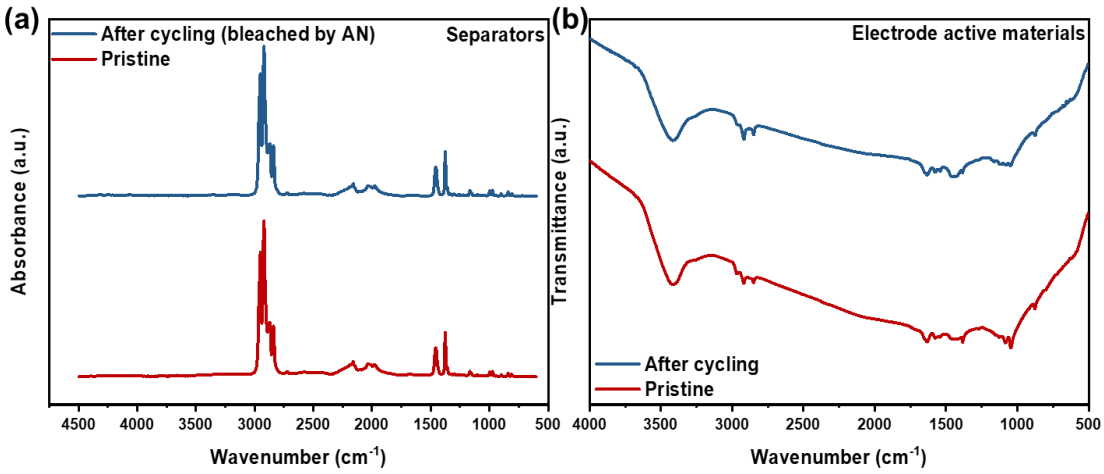

Fig. S19 (ATR-) FTIR spectra of the separators (a) and electrode active materials (b) before and after cycling.

Note: FTIR results in **Fig. S19** reveals that the electrode and separators are relatively stable after the cycling tests, which is consistent to the cycling stability results in **Fig. 3e**.

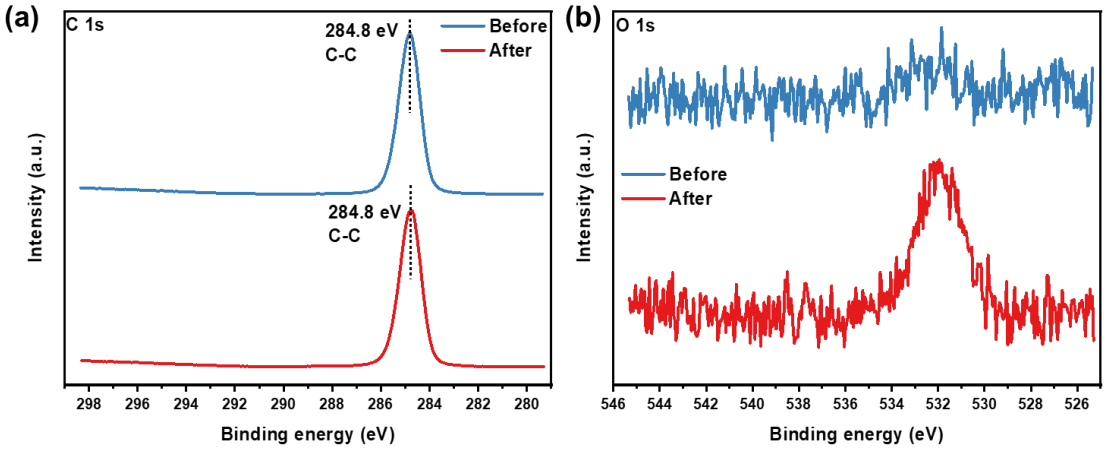

Fig. S20 XPS C 1s (a) and O 1s peaks of the separators before and after cycling.

Note: For the separators, only a small enhancement of O 1s peak appeared after the charge/discharge cycling test, revealing their considerable stability (**Fig. S20**).

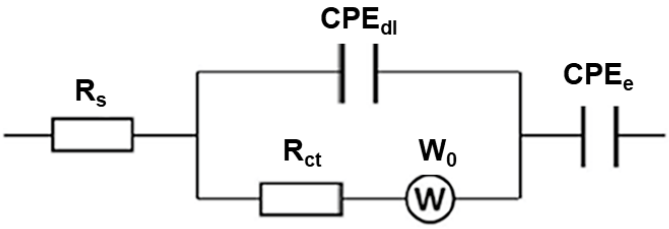

Fig. S21 Equivalent circuit for the Nyquist plots.

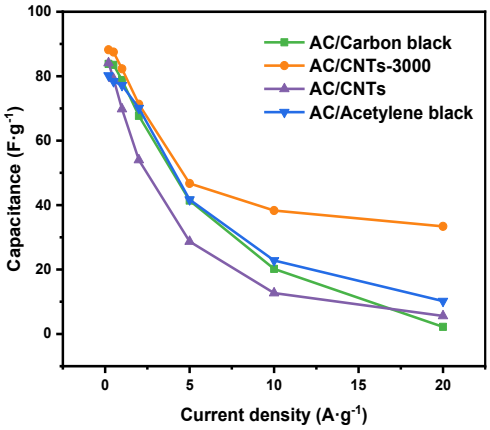

Fig. S22: Capacitance under different current densities compared with AC/Acetylene black electrode.

Note: Compared with another state-of-the-art commercialized conductive agent (acetylene black) in addition to carbon black, CNTs-3000 still exhibits better capacitance retention and more excellent rate capacity at high current density ($20A \cdot g^{-1}$).

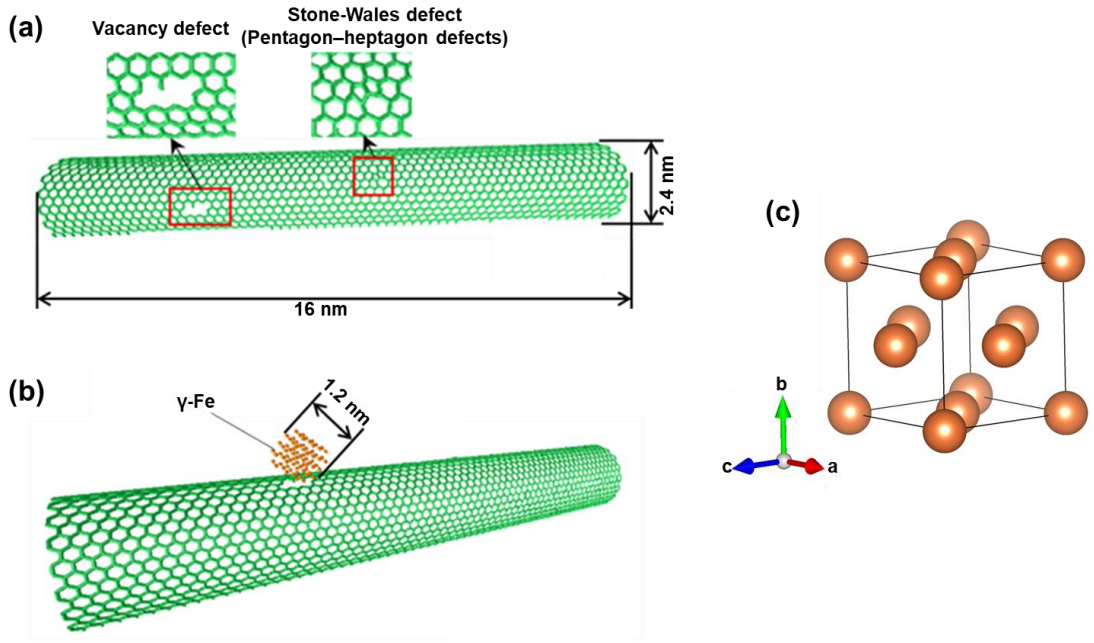

Fig. S23 (a) CNTs model with defects; (b) CNTs/γ-Fe model with defects; (c) Crystal structure of γ-Fe.

Table S1 Conductivity tests of the samples.

Samples	Conductivity ($S \cdot cm^{-1}$)
CNTs	8.70±0.43
CNTs-3000	28.57±0.25
CNTs-Fe-free	8.32±0.14
CNTs-Fe-free-3000	15.39±0.49

Note: Electrical conductivity tests shown in Table S1 revealed that without the cooperation of Fe impurities as built-in catalyst, the conductivity of CNTs after 3000 ℃ reconstruction (15.39±0.49 $S \cdot cm^{-1}$) is significantly lower than the CNTs-3000 group (28.57±0.25 $S \cdot cm^{-1}$).

Table S2: DLS results of CNTs and CNTs-3000.

Sample	Z-Average (Dh) (d, nm)	Polydispersity index (Đ)	Length (μm)	Diameter (nm)	Aspect ratio
CNTs	872.3	0.457	5.32	27	197
CNTs-3000	672.4	0.552	3.79	24	157

Note: Statistic results shown in **Table S2** revealed that after the high-temperature reconstruction, the aspect ratio of CNTs significantly decreased from ~197 to ~157, which could be attributed to the built-in catalyst that performed as the "atomic knife" that created more tips by cutting up the CNTs. Z-Average diameters tests obtained from DLS tests also revealed that the clutter size of CNTs-3000 (672.4 nm) is smaller than that of CNTs (872.3 nm), which is consistent to the tendency of tested aspect ratio, as smaller aspect ratio of CNTs will lead to weaker interweave of CNTs and smaller CNTs clutter sizes.

Table S3 Conductivity and relaxation times in LF-NMR tests of CNTs samples and other conductive agents

Samples	Conductivity ($S \cdot cm^{-1}$)	Relaxation time in LF-NMR tests (ms)
CNTs	8.70±0.43	2218.8±0.6
CNTs-3000	28.57±0.25	133.1±0.2
Carbon black	17.30±1.02	338.7±0.7
Acetylene black	20.14±0.33	429.4±0.4
Graphitized carbon spheres	11.46±0.77	328.8±0.5

Note: Compared to three commonly used electrical conductive agents (carbon black, acetylene black and graphitized carbon spheres), CNTs-3000 still exhibit superior conductivity (28.57±0.25 $S \cdot cm^{-1}$) and dispersibility (133.1±0.2 ms, relaxation time in LF-NMR tests), so although we did not prepare supercapacitors with these contrastive conductive agents additionally, we could still infer that CNTs-3000 may have a high potential for acting as a novel conductive agent.

Table S4 Conductivity and relaxation times in LF-NMR tests of CNTs samples and other conductive agents

Samples	Conductivity ($S \cdot cm^{-1}$)	Relaxation time in LF-NMR tests (ms)
CNTs	8.70±0.43	2218.8±0.6
CNTs-3000	28.57±0.25	133.1±0.2
Carbon black	17.30±1.02	338.7±0.7
Acetylene black	20.14±0.33	429.4±0.4
Graphitized carbon spheres	11.46±0.77	328.8±0.5

Table S5 data derived from the Nyquist plot.

Samples	R_s (Ω)	R_{ct} (Ω)	Warburg coefficient	R_{id} (Ω)	R^2 for σ
AC/CNTs	0.77	5.38	3.321	0.301	0.986
AC/Carbon black	0.71	3.15	2.974	0.336	0.974
AC/CNTs-3000	0.68	2.03	7.367	0.135	0.923

Note: The data shown in **Table S5** unequivocally show that the AC/CNTs-3000 electrode possesses the lowest internal resistance (R_s), indicating a highly efficient conductive network, which also exhibits the lowest charge transfer resistance (R_{ct}), demonstrating significantly faster charge transfer kinetics at the electrode/electrolyte interface and high ion diffusion efficiency. High Warburg coefficient of CNTs-3000 reveals its near-ideal capacitance behaviors.

Table S6 Conductivities and I_D/I_G values of the gradient-Fe-doped samples.

Samples	Conductivity ($S \cdot cm^{-1}$)	I_D/I_G
CNTs	8.70±0.43	1.09
CNTs-3000	28.57±0.25	0.61
CNTs-Fe-1%-3000	25.92±0.48	0.63
CNTs-Fe-5%-3000	27.44±0.34	0.61
CNTs-Fe-10%-3000	22.83±0.11	0.32

Note: The graphitization and conductivity tests of gradient-Fe-doping samples (**Fig. 2b, Fig. S7 and Table S6**) reveal that the iron-contained samples exhibit higher conductivity after the high-temperature treatment as a whole compared with primary CNTs. Particularly, CNTs-Fe-10%-3000 sample exhibits the lowest ID/IG value, indicating the highest graphitization degree. Since the conductivity of CNTs with different ratio of iron is similar, we could infer that their difference in electrochemical performance might be slight and systematic work would be carried out in the future if necessary.

Table S7 P_{max} calculated by the ESR data derived from the Nyquist plots

Devices	P_{max} (W kg^{-1})	ESR (Ω)
AC/CNT-3000 (3.5 V)	2.92×10^{5}	0.211
AC/CNT-3000 (2.7 V)	2.32×10^{4}	0.127

References

1. G. Ghanashyam and H. K. Jeong, *Chemical Physics Letters*, 2019, **725**, 31-37.
2. M. Xu, Y. H. Liu, Q. Yu, S. H. Feng, L. Zhou and L. Q. Mai, *Chinese Chemical Letters*, 2021, **32**, 184-189.
3. H. Jiang, P. S. Lee and C. Z. Li, *Energy & Environmental Science*, 2013, **6**, 41-53.
4. K. Henriksson, C. Björkas and K. Nordlund, *Journal of Physics: Condensed Matter*, 2013, **25**, 445401.